Title
A nanofabricated optoelectronic probe for manipulating and recording neural dynamics

Journal
Journal of Neural Engineering, 15(4)

ISSN
1741-2560

Authors
Li, Bingzhao
Lee, Kwang
Masmanidis, Sotiris C
et al.

Publication Date
2018-08-01

DOI
10.1088/1741-2552/aabc94

Peer reviewed

HHS Public Access

Author manuscript

J Neural Eng. Author manuscript; available in PMC 2019 August 01.

Published in final edited form as:

J Neural Eng. 2018 August 01; 15(4): 046008–. doi:10.1088/1741-2552/aabc94.

A Nanofabricated Optoelectronic Probe for Manipulating and Recording Neural Dynamics

Bingzhao Li[1,*], **Kwang Lee**[2,*], **Sotiris C. Masmanidis**[2], and **Mo Li**[1]

[1]Department of Electrical and Computer Engineering, University of Minnesota, Minneapolis, MN 55455, USA

[2]Department of Neurobiology, California Nanosystems Institute, University of California, Los Angeles, CA 90095, USA

Abstract

Objective—The convergence of optogenetic and large-scale neural recording technologies opens enormous opportunities for studying brain function. However, compared to the widespread use of optogenetics or recordings as standalone methods, the joint use of these techniques in behaving animals is much less well developed. A simple but poorly scalable solution has been to implant conventional optical fibers together with extracellular microelectrodes. A more promising approach has been to combine microfabricated light emission sources with multielectrode arrays. However, a challenge remains in how to compactly and scalably integrate optical output and electronic readout structures on the same device. Here we took a step toward addressing this issue by using nanofabrication techniques to develop a novel implantable optoelectronic probe.

Approach—This device contains multiple photonic grating couplers connected with waveguides for out-of-plane light emission, monolithically integrated with a microlectrode array on the same silicon substrate. To demonstrate the device's operation *in vivo*, we record cortical activity from awake head-restrained mice.

Main results—We first characterize photo-stimulation effects on electrophysiological signals. We then assess the probe's ability to both optogenetically stimulate and electrically record neural firing.

Significance—This device relies on nanofabrication techniques to integrate optical stimulation and electrical readout functions on the same structure. Due to the device miniaturization capabilities inherent to nanofabrication, this optoelectronic probe technology can be further scaled to increase the throughput of manipulating and recording neural dynamics.

Address for correspondence: Mo Li, 200 Union St. SE, Minneapolis, MN 55455, USA (moli@umn.edu); Sotiris Masmanidis, 650 Charles E Young Dr. South, Los Angeles, CA 90095, USA (smasmanidis@ucla.edu).

*Equal contribution

ORCID numbers:

Bingzhao Li: 0000-0001-9833-0689

Kwang Lee: 0000-0002-2689-0350

Sotiris C. Masmanidis: 0000-0002-8699-3335

Mo Li: 0000-0002-5500-0900

DISCLOSURES

The authors declare the absence of any conflict of interest.

1. INTRODUCTION

The development of optogenetics represents one of the most significant technical advances in neuroscience in recent decades [1]. It has transformed our ability to manipulate genetically and anatomically defined brain circuits with high temporal precision, and to causally examine how those circuits contribute to behavior [2]. Just as importantly, it has, in combination with complementary approaches, provided ways to greatly enhance our understanding of neural dynamics during behavior [3]. For example, together with *in vivo* electrophysiology, optogenetics enables identification of specific cell types via photo-tagging [4]. Additionally, optogenetic perturbations can be used to causally examine the influence of specific brain circuit elements or pathways on neural dynamics and computation [5]. A prerequisite for such applications is the ability to simultaneously deliver light and monitor the resulting changes in neural activity *in vivo*. Efforts to develop such multifunctional tools began to be underway shortly after the introduction of optogenetics, and have grown steadily since then [6]. On one hand, a simple approach has been to attach conventional optical fibers to microlectrodes [7–13]. While this has the advantage of being straightforward to construct, it has several limitations with regard to scalability, tissue damage if both optical fibers and electrodes are inserted in the same brain region, and the ability to control the geometry of light emission. On the other hand, micro and nanofabrication techniques offer the prospect of manufacturing compact, scalable and fully integrated optoelectronic probes [14]. There has already been substantial progress in this area. A number of approaches for combining miniature light sources with electrodes have been demonstrated, including microfabricated waveguides [15, 16] and light emitting diodes (LEDs) [17, 18]. However, the widespread adoption of such monolithically integrated systems remains limited, suggesting there may be a need to further improve certain aspects of optoelectronic probe technology.

Here we address one such need, that the probes be scalable to large numbers of recording sites that are within effective range of a light source. Microfabricated multielectrode technology (*e.g.*, silicon probes) has advanced to the level of hundreds of recording sites, providing simultaneous measurements of hundreds of neurons from behaving mice [19, 20]. We anticipate that if such multielectrode arrays could be integrated with multiple local light delivery systems, this would dramatically enhance their functionality [9]. Toward this goal, we introduce a nanofabricated optoelectronic probe relying on electron beam lithography to pattern 6 sites for optical stimulation and 40 sites for electrical recording. We demonstrate the operation of this device *in vivo* by stimulating and recording neurons in the mouse secondary motor cortex (M2). This technical advance offers a path to scaling up the recording throughput and light delivery capabilities of optoelectronic probes using nanofabrication approaches and integrated nanophotonics technologies.

2. MATERIALS AND METHODS

2.1 Optoelectronic probe fabrication

The device is fabricated through a combination of micromachining and nanofabrication processes. The implantable silicon prongs contain a layer of photonic structures made of silicon nitride (SiN), an electrical layer comprising the metallic electrodes and wires, and

isolation and encapsulating layers of silicon dioxide (SiO_2). The starting material is a silicon on insulator (SOI) wafer with a 1.2 μm thick SiO_2 layer and a 20 μm thick Si layer. A 1 μm thick SiO_2 layer is thermally grown and a 200 nm thick layer of stoichiometric silicon nitride (Si_3N_4) is deposited with low-pressure chemical vapor deposition at a commercial foundry. The finished probe contains 8 layers with a total prong thickness of 23.5 μm.

The first step of the fabrication process is to pattern the photonic structures [21], including the grating couplers and waveguides, on the SiN layer with an electron beam lithography tool (Raith EBPG 5000+) and using ZEP-520A resist. The SiN layer is then etched in an inductively coupled reactive ion etcher (Oxford ICP-RIE 100) using CHF_3 and O_2 gases. To isolate the photonic structures from the electrical layer above them, a layer of 1 μm thick SiO_2 is deposited using plasma enhanced chemical vapor deposition (PECVD). The electrical layer is fabricated with another step of electron beam lithography and the lift-off method to pattern electrodes, conduits, and wire bonding pads comprised of 10 nm thick titanium and 120 nm thick gold. Another layer of 500 nm thick SiO_2 is deposited with PECVD as the encapsulating layer to protect the electrical layer. Windows in the SiO_2 layer are etched using buffered oxide etchant (BOE) over the electrodes and pads to expose the gold layer for recording and wire bonding. Subsequently, the profile of the probe is patterned with UV photolithography and then etched from the top of the wafer to reach the base of the silicon layer, using RIE with fluorine gases for the SiN and SiO_2 layers, and the Bosch process for the silicon layer. To release the probes from the wafer, we completely etch away the backside of the wafer with the Bosch process using a deep trench etcher. To do this, the wafer is mounted on another carrier wafer covered with an etch-resistant polymer coating (ProTEK SR). Finally, the probes are released from the carrier wafer by dissolving the protection polymer and picked up from the solution with a micro-vacuum picker.

Figure 1 shows the finished probe, with two 5.2 mm long, 100 μm wide implantable prongs with center-to-center spacing of 200 μm, attached to a base for optical and electrical assembly. Each prong contains 3 optical output grating couplers with a spacing of 300 μm which are coupled to a single waveguide and an optical input grating coupler, in addition to 20 independently addressable recording electrodes with a spacing of 42 μm. The SiN waveguides from the base to the prong are 6.2 mm long. The waveguide has a width of 300 nm, which supports only the fundamental transverse-electric (TE) mode because of the relative low refractive index of stoichiometric SiN of ~1.7. Previously we found that though silicon-rich SiN has a higher refractive index and lower stress[22], it has a high absorption in the green to blue optical band commonly used in optogenetics [21]. The three grating couplers are coupled to the waveguide using directional couplers designed with the coupling efficiency to equally split the optical power. As shown in Figure 1C, the grating couplers have a uniform grating with a period of 350 nm and a duty cycle of 80%, optimized for coupling 532 nm light. Using a horn-shaped focusing design, they have a compact footprint of 16 μm × 20 μm. The size of the electrodes is 20 μm ×20 μm and the exposed window on each electrode, representing the total planar recording surface area, is 10 μm × 10 μm (Figure 1D). The electrodes are connected to the base with 1 μm wide electrical wires, though our use of electron beam lithography allows for the development of submicron wires [23].

2.2 Probe assembly and optical characterization

To create an electrical and optical interface for the probe it is mounted onto a printed circuit board (PCB), as shown in Figure 2A. Electrical connections are made with wire bonding. To couple optical fibers with the planar grating couplers, we used an in-line coupling element (ICE) (PLC Connections), which is commonly used to interface fiber optics with silicon photonic chips in telecommunication applications. A 532 nm CW laser (Optoengine LLC) is coupled to a single-mode polarization-maintaining fiber (Nufern PM460-HP) with a PC connector using an achromatic fiber collimator (Thorlabs) with a coupling efficiency of 50% (3 dB). The other end of the fiber is connected to the ICE, which is aligned to the input grating coupler on the base of the probe. Since the grating coupler is designed to couple the TE mode of the waveguide, a quarter waveplate is used to optimize the polarization of the output of the ICE to maximize the coupling efficiency. The ICE is aligned to the input grating coupler with a micromanipulator, while the optical power output from the other end of the probe is collected with a high numerical aperture objective lens, and measured with a photodetector (Thorlabs S120C). When optimal alignment is achieved (*i.e.*, when the total output power is maximized), a drop of UV curable optical epoxy (Norland NOA 61) is applied to permanently bond the ICE to the PCB. While the epoxy is curing under UV illumination, the alignment of the ICE is further finely adjusted to compensate for any shift during the curing process. We coupled the ICE to the input grating coupler of a single prong, with the waveguide on the other prong remaining un-illuminated (Figure 2B) as a control. The same configuration was used during recording. The measured optical output power thus corresponds to the total power from 3 grating couplers on one prong (Figure 2B). We estimated the power from each grating coupler by dividing the total by 3. The grating couplers emit light in collimated beams with a 10° angle perpendicular to the probe insertion axis (Figure 2C).

Our calibration measurements indicate that the overall transmission efficiency from the laser to the output end of the probe is about 0.6%, or −22.2 dB. The total optical loss includes 3 dB coupling loss between the laser and fiber, and 3 dB loss from the fiber to the ICE output. The SiN waveguide has a measured propagation loss of 3 dB/cm [21] so the total loss in the 6.2 mm long waveguide can be estimated to be 1.86 dB. Because of its symmetric design, the output grating couplers emit light in both upward and downward directions out of the plane of the probe, but both contribute to optical stimulation. They may have small internal reflection back to the waveguide. Therefore, the majority of the optical loss occurs between the ICE and input grating coupler, which amounts to about 14 dB. This loss can be reduced significantly with optimized grating coupler design and more precise ICE alignment during the epoxy curing process. Grating couplers developed for optical telecommunications has achieved less than 1 dB loss using, for example, shallow etched gratings [24] and gratings with an overlay layer [25]. Despite the relatively high overall loss, the probes still deliver sufficient optical power to achieve reliable optogenetic stimulation.

2.3 Probe electroplating and cleaning

Prior to the first *in vivo* measurement the recording sites were electroplated with gold to a final impedance of 0.1 – 0.5 MΩ (1,000 Hz) [23]. In a typical probe, we found 38 out of 40 electrodes to be electrically functional. Between each day of recording, the probe was

cleaned by immersing in trypsin solution (ThermoFisher Scientific) for at least 20 min and then rinsing with deionized water.

2.4 Animal surgery

All animal procedures were approved by the University of California, Los Angeles Chancellor's Animal Research Committee, and carried out at UCLA. Male C57BL/6J, 8 – 11 week mice were obtained from The Jackson Laboratory, and group housed in an onsite vivarium with a 12 hr light-dark cycle until the first surgery, after which they were singly housed. Surgical procedures were carried out under aseptic conditions and isoflurane anesthesia on a stereotaxic apparatus (Kopf Instruments). In the first surgery we attached a rectangular stainless steel head mounting bar on the each side of the skull (laser cut at Fab2Order). Adeno-associated virus (AAV) was obtained from the University of North Carolina Vector Core. For the Chrimson$^+$ and YFP$^+$ groups (n = 2 mice per group), we respectively injected 250 nL of undiluted AAV5-Syn-ChrimsonR-tdTomato, and AAV5-CaMKIIa-eYFP. Injections were carried out in M2 at the coordinates 2.5 mm anterior, 1.5 mm lateral, and 1.2 mm ventral from bregma. Analgesics (ibuprofen) and antibiotics (amoxicillin) were administered in the drinking water for the first week post-operatively. After 2 – 3 wks to allow time for viral expression, a second surgery under isoflurane anesthesia was performed to prepare craniotomies for electrophysiological recording. A rectangular craniotomy was made above M2, and the dura was carefully removed. An additional craniotomy was created over the posterior cerebellum for placement of a silver/silver-chloride electrical reference wire. The craniotomies were sealed with a silicone elastomer (Kwik-Cast, World Precision Instruments) until the time of recording. After a 6 hr recovery period, awake animals were placed on the head restraint apparatus, and the elastomer sealant was removed from the craniotomies. Subsequently, the probe was inserted in the brain under the control of a motorized micromanipulator (Sutter Instruments), at the coordinates 2.4 – 2.5 mm anterior, 1.4 – 1.6 mm lateral, and 2.0 mm ventral from bregma. Mineral oil was applied on the craniotomy to prevent drying. In order to increase the total number of recorded units, for each animal we performed recordings at up to 6 slightly different locations in the same viral injection zone, varying the anterior and lateral positions by 0.05 – 0.1 mm.

2.5 Data acquisition and processing

Recordings were carried out in awake head-restrained animals. The optical intensity was calibrated at the start of each recording session. After inserting the probe we waited 45 min for tissue to settle before commencing data acquisition. Recordings contained 40 trials at each of 4 different optical output power settings (3.3, 33, 66, 132 μW total across the 3 output grating couplers, corresponding to 1.1, 11, 22, 44 μW per coupler). Since the surface area of each grating coupler is 1.68×10^{-4} mm^2, the corresponding emission intensity at the surface of each grating coupler is estimated as 6.55, 65.5, 131, 262 mW/mm^2. Each trial consisted of a 100 ms continuous pulse of light, followed by an intertrial interval of 10 s. Electrophysiological signals were recorded at a sampling rate of 25,000 Hz, amplified (200 x), filtered (0.1 – 8,000 Hz), and multiplexed (32:1) on a custom head stage described previously [19]. Signals were processed offline by first removing common background activity and then bandpass filtering. Background activity was calculated as the average time-

varying voltage across all functional electrodes on a prong. This common signal was then subtracted from the voltage measured at each electrode located on that prong. The resulting signals were filtered from 600 – 6,500 Hz. Single-unit spike sorting was carried out using a custom Matlab algorithm developed previously using a spike template-matching method [19]. Spikes were detected as local voltage minima (threshold of −30 μV, corresponding to a signal-to-noise ratio of at least 4:1).

2.6 Photoelectric artifact correction

A common issue with metallic extracellular electrodes is their sensitivity to light [26, 27]. In our measurements, after bandpass filtering the signals from 600 – 6,500 Hz, photoelectric effects were confined to a brief period (~1 ms) during laser onset and offset, corresponding to the times when light intensity varied rapidly (Figures 3A and 3B insets). Some of these artifacts resemble neuronal action potentials, which raises a potential concern of detecting spurious spikes. Therefore, to correct for such photoelectric effects we excluded all threshold-crossing voltage minima events occurring within ±0.25 ms of laser onset and offset. This correction was applied to all data shown in the Results section.

2.7 Analysis of photo-stimulation effects on spike waveforms and noise

To examine whether optical stimulation influences the measured action potential shape, for each single-unit we calculated the mean waveform of spikes detected from 0 to 1 s relative to laser onset (“baseline waveform”), and spikes detected from 0 to 0.1 s relative to laser onset (“laser waveform”). The waveform duration was 1.64 ms, centered on the spike trough. As described above, spikes occurring within ±0.25 ms of laser onset were excluded from the analysis. We then calculated the Pearson correlation coefficient between the baseline and laser waveforms [28]. To examine whether optical stimulation impacts the electrical noise level, for each recording site we calculated the standard deviation (SD) of the voltage from −0.1 to 0 s relative to laser onset (“baseline”), and the SD of the voltage from 0 to 0.1 s relative to laser onset (“laser on”). In the noise analysis we removed transient photoelectric effects by excluding data within ±1 ms of laser onset.

2.8 Analysis of neural activity dependence on optical intensity

Time-varying firing rate was calculated by binning single-unit spike times in steps of 0.2 ms, and convolving with a Gaussian filter (SD = 1 ms). The change in firing rate caused by optical stimulation was calculated separately for each unit, as the difference in mean rate between 0 to 0.1 s relative to laser onset (“laser period rate”), and −1 to 0 s relative to laser onset (“baseline rate”). If a unit’s activity during the laser period exceeded 3 SD of its baseline rate, it was counted as being significantly excited. The latency to firing was calculated as the time for a unit to reach 2.5 SD of the baseline rate.

3. RESULTS

3.1 In vivo recording during optical stimulation

To evaluate the performance of the device we carried out recordings in mouse M2 that virally expressed either Chrimson [29], which depolarizes cells in the presence of light, or YFP, which served as a control (n = 2 mice per group). Control recordings were needed in

order to characterize photo-stimulation effects on electrical signals and neural activity, in the absence of any optogenetic phenomena. To maximize the yield of measured neurons, we performed recordings at multiple locations in the virus injection zone of each animal. Across all recording sessions we recorded from 56 single-units in the Chrimson$^+$ group, and 50 units in the YFP$^+$ group, with a yield of 7 ± 5 (mean ± SD, range: 1 – 13) units per session. Optical illumination was applied continuously for 100 ms at 4 different intensity levels (40 trials per intensity setting, 10 s intertrial interval).

During the laser stimulus we found electrodes which showed a noticeable increase in spiking activity in the Chrimson$^+$ group (Figure 3A). As expected, there did not appear to be a corresponding increase in spiking in the YFP$^+$ group (Figure 3B). In both groups we also observed fluctuations of several hundred microvolts in the filtered signal (600 – 6,500 Hz) during laser onset and offset, consistent with photoelectric effects that occur on metallic electrodes [26]. Some of these artifacts resemble extracellular action potentials, raising the possibility that these events could be spuriously detected as spikes, thus contaminating the data. To mitigate this potential problem, we took advantage of the transient nature of photoelectric artifact signals, and excluded any spike-like signals detected within ±0.25 ms of laser onset and offset (Figures 3A and 3B insets). Since neuronal response times to Chrimson-mediated stimulation typically exceed 1 ms [29], our exclusion criterion is unlikely to significantly impact the analysis of neural activity. Furthermore, for a hypothetical cell firing at 10 Hz the probability that it will fire a spike during the exclusion period around laser onset is just $10\ s^{-1} \times 0.0005\ s = 0.5\ \%$. Therefore, our approach to correcting for photoelectric artifacts is unlikely to adversely impact the results.

To determine whether the laser stimulus caused any other unwanted distortions in the electrophysiological signals which could confound the data analysis, we compared the mean spike waveform of each unit during laser off and on conditions (Figure 3C) [28]. There was a high correlation ($r > 0.95$) between the mean laser off and on waveforms, indicating that for the majority of measured units the optical stimulus did not significantly alter the shape of extracellular action potentials (Figures 3D, 3E). We also examined the extent to which the laser altered the total root-mean-square noise level measured *in vivo*. Across all electrode recording sites (n = 38 channels) we found a statistically significant increase in noise (paired t-test, Chrimson$^+$ group: $p = 0.026$, Figure 3F; YFP$^+$ group: $p = 0.012$, Figure 3G). However, the increase was small – less than 1 μV, which is low relative to the total noise. Since the lowest action potential amplitude was set to 30 μV, the optically induced noise increase does not appear to influence the ability to detect spikes in these measurements. Taken together, the results show that the optoelectronic probe is capable of recording spiking activity during optogenetic stimulation, with relatively little signal distortion.

3.2 Dependence of neural activity on optical intensity

Next we examined how neural activity was modulated by stimulation at different light intensities. On a subset of units in the Chrimson$^+$ group, spiking intensified at higher emission intensity (Figure 4A) with the threshold for activation between 65.5 – 131 mW/mm^2. Across all units in the Chrimson$^+$ group, the optically evoked change in firing rate scaled positively with emission intensity (Figure 4B). In contrast, firing rate in the YFP$^+$

group did not increase under higher intensity, and in fact there was a small but statistically significant decline in firing at the highest intensity setting (Figure 4C). The fraction of significantly excited cells was also higher in the Chrimson$^+$ compared to the YFP$^+$ group (Figure 4D). The fraction of significantly excited cells appeared to saturate beyond an intensity of 131 mW/mm^2. We also noted a small reduction in the fraction at higher intensity, but the difference between the values at 131 mW/mm^2 (16.1 % of 56 = 9 cells) and 262 mW/mm^2 (14.3 % of 56 = 8 cells) was not statistically significant (chi squared test, $p > 0.99$). Finally, we characterized the response time of significantly excited units to optical stimulation (n = 8 units in the Chrimson$^+$ group, Figure 4E). The latency of evoked firing at 131 mW/mm^2 was 18 ± 10.5 ms (mean ± SD), and at 262 mW/mm^2 the latency was significantly reduced to 10.4 ± 5.9 ms (paired t-test, $p = 0.008$, Figure 4F). Together, these results demonstrate that the optoelectronic probe can simultaneously manipulate and monitor neural activity in the awake mouse motor cortex.

4. DISCUSSION

The rapidly growing field of neurophotonics is seeing promising demonstrations of integrated optical and electrical microstructures for optogenetic stimulation and recording [6]. However, an enduring challenge is scalability – how to increase the number of optical emission and electrical recording sites. Here we have presented a potential path to resolving this issue, using electron beam lithography to produce nanofabricated optical and electrical device features. Due to the narrow width of the optical waveguides and electrical wires, the number of stimulation and recording sites can be scaled up without requiring a correspondingly larger and thus more invasive silicon probe [23, 30–32]. Even though electron beam lithography is used, the critical dimensions of both the optical and the electrical components of the probe are well within the range of deep UV lithography so they can be produced in mass quantities at commercial semiconductor foundries [19], facilitating widespread dissemination. This technology has numerous applications in neuroscience including optogenetic tagging, and examining how genetically and anatomically defined circuits regulate animal behavior, neural activity, and computation.

Light emission in our device relies on an external source of (laser) illumination, coupled to the optical waveguides on the probe via an optical fiber and ICE. These coupling elements are commercially available, which could help facilitate the widespread distribution of the optoelectronic probe technology in the future. It is also straightforward to scale up the number of light emission sites that are coupled to the external laser [33], enabling optogenetic stimulation of larger populations of neurons. However, a potential disadvantage of using an external light source is the limited number of independently addressable optical channels. The probe presented here emits light from all emission sites simultaneously. This simplifies the assembly process, but restricts the spatial selectivity of light. We therefore anticipate that the scalability of our technology will be most useful in applications requiring widespread illumination to optogenetically stimulate as many neurons as possible near the electrical recording sites [10]. In contrast, local sources of light such as micro-LED arrays patterned directly on the implanted probe are likely to be better suited for applications requiring dynamically configurable spatially patterned illumination [17, 34]. Alternatively, instead of using an ICE to couple light from external lasers, LEDs or laser diode (LD) arrays

could be mounted directly on the PCB. This method has the advantage of avoiding the high optical losses occurring between the ICE and grating coupler. Using LED/LDs on the PCB also lowers the overall cost of manufacturing. Each LED/LD can be coupled to a separate waveguide and controlled separately to enable dynamic spatial control of the light emission.

A common problem with combining optogenetics with metallic extracellular electrodes is the presence of photoelectric artifacts during optical stimulation. While these artifacts were also present in measurements with our probe, in the spike frequency range they were confined to a ~millisecond period around the onset and offset of the optical pulse – a timescale that is shorter than the typical latency of neural activation. We therefore estimate that photoelectric effects in these probes will not pose a significant problem for long duration and low frequency (duration greater than ~50 ms and frequency less than ~10 Hz) light pulses. However, shorter duration or higher frequency pulses may significantly interfere with our ability to measure single-unit spikes. In those applications, non-metallic electrodes and polymer-based substrates, which do not exhibit photoelectric effects, may be more favorable [14, 18, 35].

In conclusion, this is one of the first optoelectronic probes to use nanofabrication techniques to integrate optical stimulation and electrical readout functions on the same structure. The miniaturization capabilities afforded by these fabrication methods offer the prospect for developing a scaled up version of this multifunctional device for massively parallel optogenetic manipulation and electrical recording of neural dynamics.

Acknowledgments

S.C.M. was supported by NSF CBET 1263785, NSF NeuroNex Technology Hub Award 1707408, NIH DA034178, NIH NS100050, and NIH DA042739. M.L. was supported by NSF CBET 1263987 and a Faculty Career Development Award from the Institute of Engineering in Medicine of the University of Minnesota. Parts of this work were carried out in the University of Minnesota Nanofabrication Center which receives partial support from NSF through NNIN program, and the Characterization Facility which is a member of the NSF funded Materials Research Facilities Network via the MRSEC program.

References

1. Boyden ES, Zhang F, Bamberg E, Nagel G, Deisseroth K. Millisecond-timescale, genetically targeted optical control of neural activity. Nature Neuroscience. 2005; 8:1263–8. [PubMed: 16116447]
2. Zhang F, Aravanis AM, Adamantidis A, de Lecea L, Deisseroth K. Circuit-breakers: optical technologies for probing neural signals and systems. Nat Rev Neurosci. 2007; 8:577–81. [PubMed: 17643087]
3. Kim CK, Adhikari A, Deisseroth K. Integration of optogenetics with complementary methodologies in systems neuroscience. Nat Rev Neurosci. 2017; 18:222–35. [PubMed: 28303019]
4. Lima SQ, Hromadka T, Znamenskiy P, Zador AM. PINP: a new method of tagging neuronal populations for identification during in vivo electrophysiological recording. PLoS One. 2009; 4:e6099. [PubMed: 19584920]
5. Lee SH, Kwan AC, Zhang S, Phoumthipphavong V, Flannery JG, Masmanidis SC, Taniguchi H, Huang ZJ, Zhang F, Boyden ES, Deisseroth K, Dan Y. Activation of specific interneurons improves V1 feature selectivity and visual perception. Nature. 2012; 488:379–83. [PubMed: 22878719]
6. Iseri E, Kuzum D. Implantable optoelectronic probes for in vivo optogenetics. J Neural Eng. 2017; 14:031001. [PubMed: 28198703]

7. Gradinaru V, Thompson KR, Zhang F, Mogri M, Kay K, Schneider MB, Deisseroth K. Targeting and readout strategies for fast optical neural control in vitro and in vivo. J Neurosci. 2007; 27:14231–8. [PubMed: 18160630]
8. Royer S, Zemelman BV, Barbic M, Losonczy A, Buzsaki G, Magee JC. Multi-array silicon probes with integrated optical fibers: light-assisted perturbation and recording of local neural circuits in the behaving animal. Eur J Neurosci. 2010; 31:2279–91. [PubMed: 20529127]
9. Buzsaki G, Stark E, Berenyi A, Khodagholy D, Kipke DR, Yoon E, Wise KD. Tools for probing local circuits: high-density silicon probes combined with optogenetics. Neuron. 2015; 86:92–105. [PubMed: 25856489]
10. Lee K, Holley SM, Shobe JL, Chong NC, Cepeda C, Levine MS, Masmanidis SC. Parvalbumin Interneurons Modulate Striatal Output and Enhance Performance during Associative Learning. Neuron. 2017; 93:1451–63 e4. [PubMed: 28334608]
11. Wang J, Wagner F, Borton DA, Zhang J, Ozden I, Burwell RD, Nurmikko AV, van Wagenen R, Diester I, Deisseroth K. Integrated device for combined optical neuromodulation and electrical recording for chronic in vivo applications. J Neural Eng. 2012; 9:016001. [PubMed: 22156042]
12. Aravanis AM, Wang LP, Zhang F, Meltzer LA, Mogri MZ, Schneider MB, Deisseroth K. An optical neural interface: in vivo control of rodent motor cortex with integrated fiberoptic and optogenetic technology. J Neural Eng. 2007; 4:S143–56. [PubMed: 17873414]
13. Stark E, Koos T, Buzsaki G. Diode probes for spatiotemporal optical control of multiple neurons in freely moving animals. J Neurophysiol. 2012; 108:349–63. [PubMed: 22496529]
14. Zorzos AN, Boyden ES, Fonstad CG. Multiwaveguide implantable probe for light delivery to sets of distributed brain targets. Opt Lett. 2010; 35:4133–5. [PubMed: 21165114]
15. Son Y, Lee HJ, Kim J, Shin H, Choi N, Lee CJ, Yoon ES, Yoon E, Wise KD, Kim TG, Cho IJ. In vivo optical modulation of neural signals using monolithically integrated two-dimensional neural probe arrays. Scientific reports. 2015; 5:15466. [PubMed: 26494437]
16. Wu F, Stark E, Im M, Cho IJ, Yoon ES, Buzsaki G, Wise KD, Yoon E. An implantable neural probe with monolithically integrated dielectric waveguide and recording electrodes for optogenetics applications. J Neural Eng. 2013; 10:056012. [PubMed: 23985803]
17. Wu F, Stark E, Ku PC, Wise KD, Buzsaki G, Yoon E. Monolithically Integrated muLEDs on Silicon Neural Probes for High-Resolution Optogenetic Studies in Behaving Animals. Neuron. 2015; 88:1136–48. [PubMed: 26627311]
18. Kim TI, McCall JG, Jung YH, Huang X, Siuda ER, Li Y, Song J, Song YM, Pao HA, Kim RH, Lu C, Lee SD, Song IS, Shin G, Al-Hasani R, Kim S, Tan MP, Huang Y, Omenetto FG, Rogers JA, Bruchas MR. Injectable, cellular-scale optoelectronics with applications for wireless optogenetics. Science. 2013; 340:211–6. [PubMed: 23580530]
19. Shobe JL, Claar LD, Parhami S, Bakhurin KI, Masmanidis SC. Brain activity mapping at multiple scales with silicon microprobes containing 1,024 electrodes. Journal of Neurophysiology. 2015; 114:2043–52. [PubMed: 26133801]
20. Jun JJ, Steinmetz NA, Siegle JH, Denman DJ, Bauza M, Barbarits B, Lee AK, Anastassiou CA, Andrei A, Aydin C, Barbic M, Blanche TJ, Bonin V, Couto J, Dutta B, Gratiy SL, Gutnisky DA, Hausser M, Karsh B, Ledochowitsch P, Lopez CM, Mitelut C, Musa S, Okun M, Pachitariu M, Putzeys J, Rich PD, Rossant C, Sun WL, Svoboda K, Carandini M, Harris KD, Koch C, O'Keefe J, Harris TD. Fully integrated silicon probes for high-density recording of neural activity. Nature. 2017; 551:232–6. [PubMed: 29120427]
21. Shim E, Chen Y, Masmanidis S, Li M. Multisite silicon neural probes with integrated silicon nitride waveguides and gratings for optogenetic applications. Scientific reports. 2016; 6:22693. [PubMed: 26941111]
22. Gorin A, Jaouad A, Grondin E, Aimez V, Charette P. Fabrication of silicon nitride waveguides for visible-light using PECVD: a study of the effect of plasma frequency on optical properties. Opt Express. 2008; 16:13509–16. [PubMed: 18772959]
23. Du J, Blanche TJ, Harrison RR, Lester HA, Masmanidis SC. Multiplexed, high density electrophysiology with nanofabricated neural probes. PLoS One. 2011; 6:e26204. [PubMed: 22022568]

24. Taillaert D, Bienstman P, Baets R. Compact efficient broadband grating coupler for silicon-on-insulator waveguides. Opt Lett. 2004; 29:2749–51. [PubMed: 15605493]
25. Roelkens G, Van Thourhout D, Baets R. High efficiency Silicon-on-Insulator grating coupler based on a poly-Silicon overlay. Opt Express. 2006; 14:11622–30. [PubMed: 19529582]
26. Kravitz AV, Owen SF, Kreitzer AC. Optogenetic identification of striatal projection neuron subtypes during in vivo recordings. Brain Res. 2013; 1511:21–32. [PubMed: 23178332]
27. Cardin JA, Carlen M, Meletis K, Knoblich U, Zhang F, Deisseroth K, Tsai LH, Moore CI. Targeted optogenetic stimulation and recording of neurons in vivo using cell-type-specific expression of Channelrhodopsin-2. Nat Protoc. 2010; 5:247–54. [PubMed: 20134425]
28. Cohen JY, Haesler S, Vong L, Lowell BB, Uchida N. Neuron-type-specific signals for reward and punishment in the ventral tegmental area. Nature. 2012; 482:85–8. [PubMed: 22258508]
29. Klapoetke NC, Murata Y, Kim SS, Pulver SR, Birdsey-Benson A, Cho YK, Morimoto TK, Chuong AS, Carpenter EJ, Tian Z, Wang J, Xie Y, Yan Z, Zhang Y, Chow BY, Surek B, Melkonian M, Jayaraman V, Constantine-Paton M, Wong GK, Boyden ES. Independent optical excitation of distinct neural populations. Nature methods. 2014; 11:338–46. [PubMed: 24509633]
30. Rios G, Lubenov EV, Chi D, Roukes ML, Siapas AG. Nanofabricated Neural Probes for Dense 3-D Recordings of Brain Activity. Nano Lett. 2016; 16:6857–62. [PubMed: 27766885]
31. Segev E, Reimer J, Moreaux LC, Fowler TM, Chi D, Sacher WD, Lo M, Deisseroth K, Tolias AS, Faraon A, Roukes ML. Patterned photostimulation via visible-wavelength photonic probes for deep brain optogenetics. Neurophotonics. 2017; 4:011002. [PubMed: 27990451]
32. Scholvin J, Kinney JP, Bernstein JG, Moore-Kochlacs C, Kopell N, Fonstad CG, Boyden ES. Close-Packed Silicon Microelectrodes for Scalable Spatially Oversampled Neural Recording. IEEE Trans Biomed Eng. 2016; 63:120–30. [PubMed: 26699649]
33. Poulton CV, Byrd MJ, Raval M, Su Z, Li N, Timurdogan E, Coolbaugh D, Vermeulen D, Watts MR. Large-scale silicon nitride nanophotonic phased arrays at infrared and visible wavelengths. Opt Lett. 2017; 42:21–4. [PubMed: 28059212]
34. Scharf R, Tsunematsu T, McAlinden N, Dawson MD, Sakata S, Mathieson K. Depth-specific optogenetic control in vivo with a scalable, high-density muLED neural probe. Scientific reports. 2016; 6:28381. [PubMed: 27334849]
35. Kuzum D, Takano H, Shim E, Reed JC, Juul H, Richardson AG, de Vries J, Bink H, Dichter MA, Lucas TH, Coulter DA, Cubukcu E, Litt B. Transparent and flexible low noise graphene electrodes for simultaneous electrophysiology and neuroimaging. Nature communications. 2014; 5:5259.

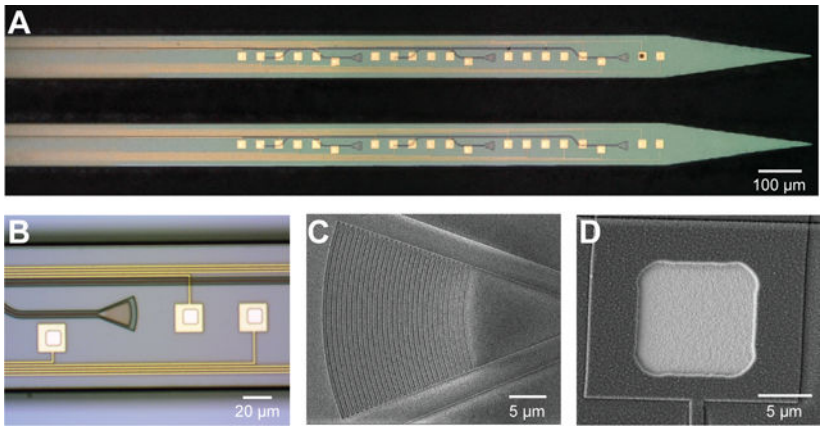

Figure 1.

Images of the optoelectronic probe and its components.

(A) Optical image of the probe.

(B) Higher magnification view of a section of the probe, showing the optical grating coupler and electrodes.

(C) Scanning electron microscope image of the SiN grating coupler.

(D) Scanning electron microscope image of the gold electrode with exposed window in the encapsulating layer of silicon dioxide.

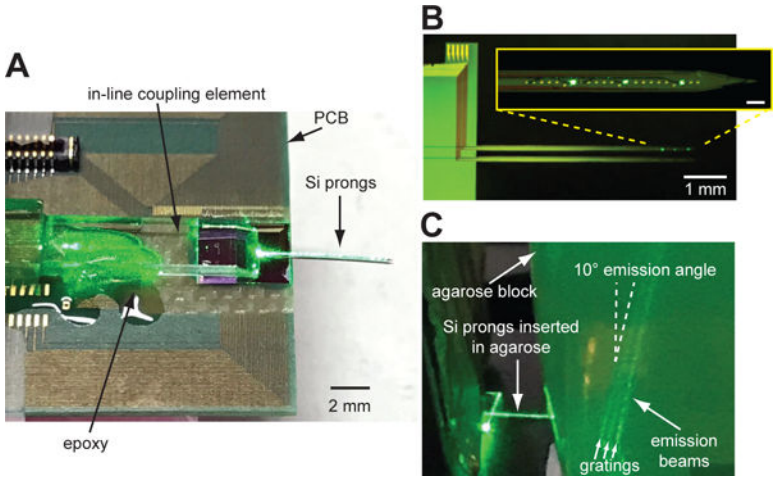

Figure 2.

Images of the assembled probe with optical output.

(A) The probe assembled on the PCB. The ICE is aligned to the probe and attached to the PCB with epoxy. The green laser is turned on at a high power to show scattered light from the probe.

(B) Dark-field optical image of the probe when the green laser is turned on. Emission from the three grating couplers can be seen. Inset shows a high magnification view of the prong coupled to the laser. Inset scale bar = 100 μm.

(C) Three emitted optical beams (one per output grating coupler) are shown to be collimated and propagating in agarose with an emission angle of 10° perpendicular to the probe insertion angle.

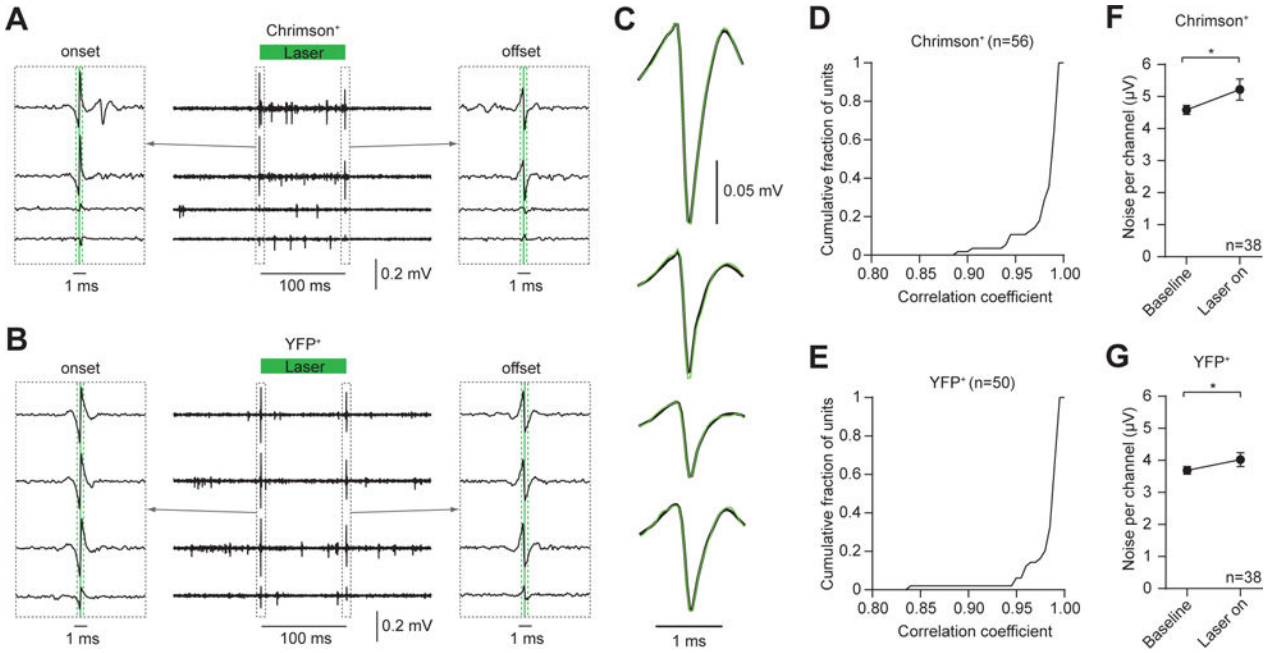

Figure 3.

Combined optical stimulation and electrical recording with the probe.

(A) Time-varying voltage of 4 channels recorded from a Chrimson$^+$ mouse, in response to a 100 ms optical stimulus. Left and right insets respectively show an expanded view of the photoelectric artifacts occurring at the time of laser onset and offset (solid green lines). The dashed green lines indicate the ±0.25 ms time windows centered on laser onset and offset, which are excluded from the analysis of spiking activity. Signals are background-subtracted and filtered from 600 – 6,500 Hz.

(B) Same as A but for 4 channels recorded from a YFP$^+$ mouse.

(C) Mean spike waveform of 4 putative units during baseline (black lines) and laser on conditions (green lines). There is a high correlation between the waveforms during baseline and laser on conditions ($r > 0.99$). The top 2 waveforms are from Chrimson$^+$ group, and the bottom 2 waveforms are from the YFP$^+$ group.

(D) Cumulative fraction of units as a function of the correlation coefficient between their waveforms during baseline and laser on conditions. Data represent n = 56 units from the Chrimson$^+$ group.

(E) Same as D but data represent n = 50 units from the YFP$^+$ group.

(F) Comparison of standard deviation of the voltage per channel during baseline and laser on conditions. Data represent mean ± standard error on the mean (SEM) of 38 channels from the Chrimson$^+$ group. The laser significantly increased the average noise level (paired t-test, $p = 0.026$).

(G) Same as F but data represent mean ± SEM of 38 channels from the YFP$^+$ group. The laser significantly increased the average noise level (paired t-test, $p = 0.012$). All data in this figure correspond to the maximum emission intensity setting (262 mW/mm^2).

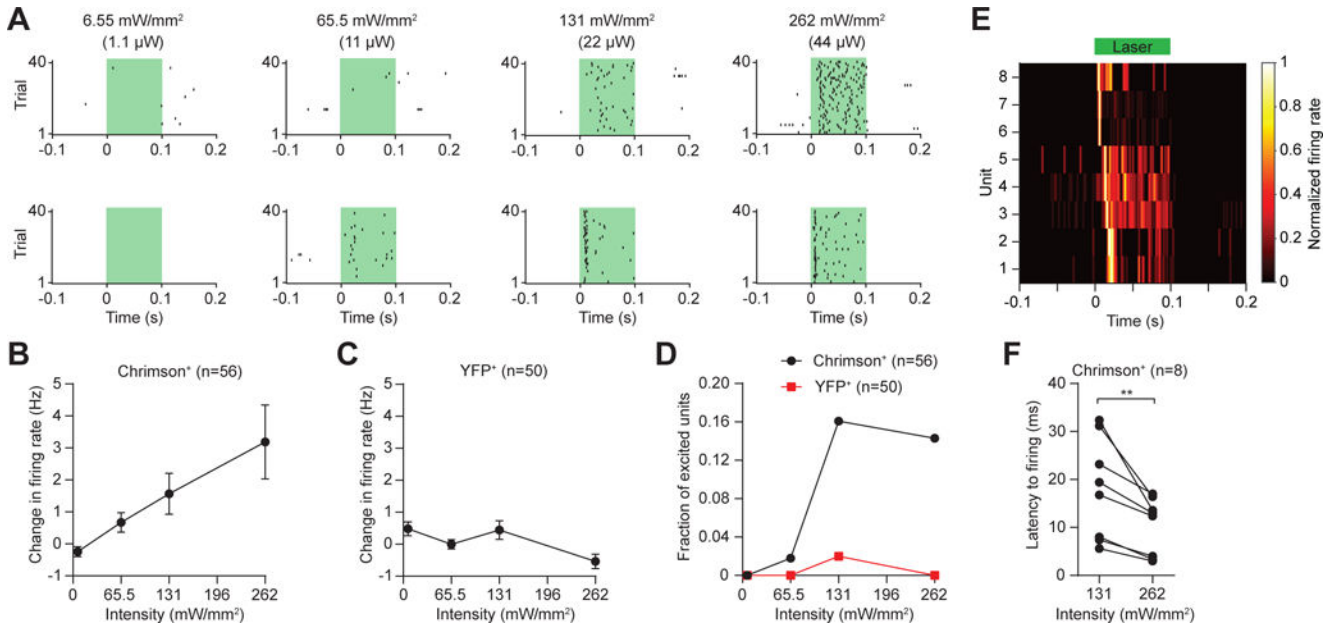

Figure 4.

Optical modulation of neural activity at different emission intensity.

(A) Spike raster of 2 units (top and bottom rows) recorded from the Chrimson$^+$ group. Each column represents a different optical emission intensity at each output grating coupler. Values in parentheses indicate the corresponding power per grating coupler.

(B) Change in firing rate during optical stimulation relative to baseline, as a function of optical intensity. Data represent n = 56 units from the Chrimson$^+$ group. There was a significant effect of intensity on firing rate (one-way repeated-measures ANOVA, F = 6.9, p = 0.006). Post-hoc multiple comparisons analysis revealed that firing rate at 6.55 mW/mm^2 was significantly lower than the rate at 65.5 mW/mm^2 (p = 0.015), 131 mW/mm^2 (p = 0.02), and 262 mW/mm^2 (p = 0.012).

(C) Same as B but data represent n = 50 units from the YFP$^+$ group. There was a significant effect of optical intensity on firing rate (one-way repeated-measures ANOVA, F = 4.1, p = 0.021). Post-hoc multiple comparisons analysis revealed that firing rate at 6.55 mW/mm^2 was not significantly different than the rate at 65.5 mW/mm^2 (p = 0.13) or 131 mW/mm^2 (p = 0.99), but was significantly higher than the rate at 262 mW/mm^2 (p = 0.008).

(D) Fraction of significantly excited units during the laser stimulation period in the Chrimson$^+$ (black) and YFP$^+$ (red) groups.

(E) Mean normalized time-varying firing rate of the 8 out of 56 units in the Chrimson$^+$ group, which were significantly excited by the laser at 262 mW/mm^2. The green bar indicates the duration of the optical stimulus. Units are plotted in order of their latency to firing.

(F) Latency to firing of the 8 units in E at an intensity of 131 and 262 mW/mm^2. There was a significant reduction in latency at higher intensity (paired t-test, p =0.008).